WPS2-PR(18) 19303

H Patten et al.

The Effect of Magnetic Topology on Auxiliary Heating Schemes and Fast Particle Confinement in Wendelstein-7X

Preprint of Paper to be submitted for publication in
Plasma Physics and Controlled Fusion

This work has been carried out within the framework of the EUROfusion Consortium and has received funding from the Euratom research and training programme 2014-2018 under grant agreement No 633053. The views and opinions expressed herein do not necessarily reflect those of the European Commission.

The Effect of Magnetic Equilibrium on Auxiliary Heating Schemes and Fast Particle Confinement in Wendelstein 7-X

H. Patten[1], J.P. Graves[1], J. Faustin[2], W.A. Cooper[1], J. Geiger[2], D. Pfefferlé[3] and Y. Turkin[2]

[1]EPFL-SPC, CH-1015 Lausanne, Switzerland
[2]Max Planck Institute for Plasma Physics, Wendelsteinstraβe 1, 17491, Greifswald, Germany
[3]Princeton Plasma Physics Laboratory, Princeton 08540 NJ, USA

Abstract

The performance of the auxiliary heating systems Ion Cyclotron Resonance Heating and Neutral Beam Injection is calculated in three different magnetic mirror configurations foreseen to be used in future experiments in the Wendelstein 7-X stellarator: low, standard and high mirror. This numerical work is implemented with the SCENIC code package, which is designed to model three-dimensional magnetic equilibria whilst retaining effects such as anisotropy and the influence of including a Finite Orbit Width of the particles. The ability to simulate NBI deposition in three-dimensional equilibria, the implementation of the realistic beam injector geometry, and the modification of the SCENIC package to permit the investigation of the 3-ion species heating scheme, are recent developments. Using these modifications, an assessment of the advantages and disadvantages of these two fast-ion producing auxiliary heating systems is made in the three different magnetic mirror equilibria. For NBI heating, the high mirror configuration displays the best global confinement properties, resulting in a larger collisional power transfer to the background plasma. The standard mirror has the best particle confinement in the core region, but the worst towards the edge of the plasma. The low mirror has the largest lost power and thus the lowest total collisional power. For ICRH, the displacement of the RF-resonant surface significantly impacts the heating performance. Due to the large toroidal magnetic mirror in the high mirror equilibrium, resonant particles easily become trapped and cannot remain in resonance, generating only small energetic particle populations. Despite this, global confinement is still the strongest in this equilibrium. The low mirror is the only equilibrium to produce peaked on-axis collisional power deposition, with associated peaked on-axis fast ion pressure profiles. A highly energetic particle population is then produced but this results in larger lost power as this equilibrium is not sufficiently optimised for fast ion confinement. A comparison between the two heating methods concludes that NBI produces a smaller fraction of lost to input power, and a reduced sensitivity of the performance to variations of the toroidal magnetic mirror. The main limit of NBI which does not apply to ICRH is the production of highly energetic particle populations, with predictions of energetic particles of $E \sim 0.45MeV$.

1 Introduction

In the development towards a commercial nuclear fusion reactor, the stellarator concept could prove to be a promising design for a steady-state device. However, in order to progress to high perfomance plasmas, optimisation of the auxiliary heating sources is required. The fast-ion generating auxiliary heating systems to be used on the Wendelstein 7-X (W7-X) stellarator, Germany, are Ion Cyclotron Resonance Heating (ICRH) and Neutral Beam Injection (NBI). These two contrasting methods have very different influences on the production of the fast-ion population. ICRH predominantly increases the particle's magnetic moment [1] and the trapping fraction, whereas the anisotropic properties of NBI produced fast ions depend on the injection angle and the beam ionisation deposition. This seemingly small difference results in very different particle orbits and directly impacts the radial diffusion and confinement of such particles. In order to optimise these two heating systems, it is also necessary to evaluate the ability of the magnetic field configuration to confine these fast-ion populations. Flexibility of the magnetic topology is achieved via a modification of the individual modular coil currents. This then leads to very different particle transport and plasma properties and therefore affects the overall performance [2].

The challenge of simulating the performance of NBI in W7-X has been recently attempted for modest values of $<\beta>=$ 2% [3, 4]. The NBI beam ionisation deposition was shown to be localised on the outer flux surfaces on the Low Field Side (LFS). Over slowing down timescales, large losses and high radial diffusion are predicted, and thermalised particles remain localised in the outer flux surfaces. Providing numerical insight into the performance of Ion Cyclotron Range of Frequency (ICRF)-wave and complicated magnetic geometry is extremely difficult and computationally expensive. Calculating the wave propagation with a fully localised antenna breaks the five-fold periodicity that is specific to W7-X. Simulations predicting the performance of minority species ICRH schemes in W7-X have been performed [5], where a comparison is made between two different magnetic topologies known as the 'standard' and 'high' mirror equilibria, (the difference between these is described in section 2.2). Due to the predominant perpendicular heating and large trapping fractions, poor confinement of resonant particles caused by ICRH was observed. Significant differences in the performance of ICRH in the high and moderate mirror equilibria were not observed (explained in section 2.2). The advanced ICRF heating scheme known as the '3-ion species' [6, 7] has also been previously explored in the high mirror equilibrium [8]. The results imply that despite developing a larger highly-energetic ion population than the minority heating scheme, the confinement of such particles is considerably worse due to increased radial excursion and reduced poloidal precession of particles among other reasons.

The aim of this paper is to explore the complicated interplay between magnetic toplogy and auxiliary heating schemes on fast ion production and confinement. The SCENIC [9] package includes a suite of several codes that permit the self consistent calculation of NBI and ICRF heating in two and three dimensional magnetic equilibria. The magnetic flux geometry is determined by the ANIMEC [10] code, including the anisotropic fast ion pressure contributions to the force balance equation. The generation of the neutral beam deposition fast ion population is performed using the VENUS NBI module [11], based on a realistic model of the three-dimensional NBI injector geometry. Calculation of the ICRF-wave propagation and absorption with a fully localised antenna is made using the LEMan [12] code. Finally, VENUS-LEVIS [13] is the Fokker Planck particle full- or guiding-centre motion following code. This includes the influence of Coulomb collisions with both energy and pitch angle scattering effects, and wave-particle resonant interactions via a Monte-Carlo based Quasi-Linear Operator (QLO).

The layout of this paper is as follows. In section 2, a simplified characterisation of the magnetic equilibrium parameters will be presented, including the influence of the equilibria on the particle guiding centre motion. Section 3 focuses on the roles of NBI heating on each of the magnetic topologies through particle deposition, radial diffusion and resultant slowing down distribution. Section 4 presents ICRH simulations with a focus on three-ion species heating [6], as well as the results from standard minority heating. Section 4 also includes an extensive study of the fast-ion distribution function and the influence of the resonance location on radial particle diffusion. The final section (5) compares the performance of the two fast ion heating methods. The total collisional power transferred to the background plasma and the lost power from the LCFS is calculated.

2 Magnetic Equilibria in W7-X

2.1 Simulation Profiles

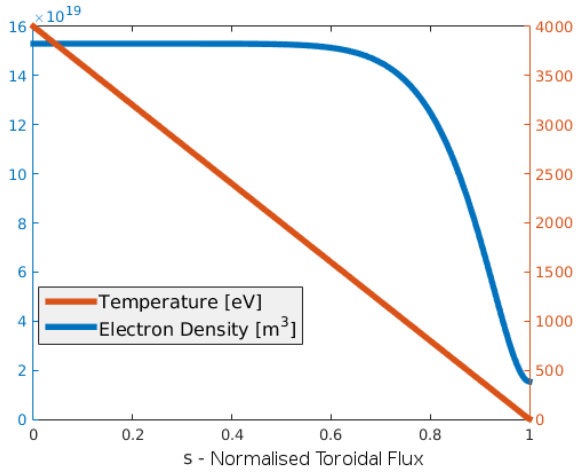

Figure 1: Background temperature and electron density profiles, with $s = \psi_{tor}/\psi_{tor,edge}$.

Within the first few campaigns, experiments at W7-X are likely to have a $\langle\beta\rangle$ value of between $2-3\%$. In these simulations, the global beta will be taken to be 3%, defined as:

$$\langle\beta\rangle = \frac{2\mu_0 \int \mathrm{p} d}{\int B^2 d}. \quad (1)$$

The temperature profiles will be mostly imposed by the usage of Electron Cyclotron Resonance Heating (ECRH) which is most efficient within the core, typically producing peaked temperature profiles. It is to be noted that the influence of ECRH cannot be simulated by the code package implemented in this work, though

its influence will remain on the background temperature profiles and the ambipolar electric field described in section 2.3. To justify the plasma profiles chosen in the simulations presented in this paper, a few considerations are made. One of the benefits of stellarators is that no plasma current is required to produce the poloidal magnetic field, and therefore the Greenwald limit [14] does not formally exist for stellarators. This permits much higher densities to form, typically with a 'flat top' shape, as shown in figure 1. The electron density profile will be held fixed according to figure 1, and the temperature profile shown in figure 1 will be applied to all background plasma species.

Throughout the experiments that will take place over the first few years at W7-X, the number of neutrons produced during each shot is to be minimised. Therefore, it is foreseen that there will be no deuterium as the background plasma element during the commisioning and early use of ICRH. Due to this, the majority background plasma species in this paper has been chosen to be helium-4 in order to permit the use of certain Ion Cyclotron Resonance Heating (ICRH) schemes, to be described in section 4. The magnetic equilibria assumed in this paper are chosen so as to advance the work of [15]. In particular, we investigate configurations with low magnetic toroidal mirror and contrast the properties with the previously studied high mirror.

The individual currents in each of the modular coil sets are modified in order to produce different magnetic topologies using VMEC [16][1]. The equilbria are generated for a variety of different plasma $\langle\beta\rangle$ values, the Last Closed Flux Surface (LCFS) shape of which can be extracted. The LCFS used in the ANIMEC code [10] was taken from the free-boundary VMEC generated equilibria with zero plasma current radial profile.

2.2 Configurations with Varying Toroidal Magnetic Mirror

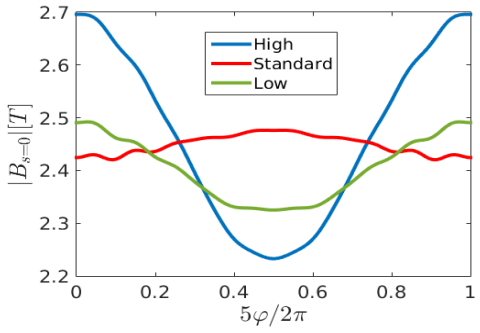

Figure 2: The magnetic field strength on axis against the toroidal boozer angle φ, for each magnetic configuration.

W7-X is a five-fold periodic stellarator. Changing the currents in each individual modular coil permits the creation of different magnetic equilibria, whereby one of the parameters often investigated is known as the toroidal magnetic mirror value, which refers to the relative strength of the toroidal variation of the magnetic field on the magnetic axis,

$$MR = \frac{B_{\varphi=0}(s=0) - B_{\varphi=\pi/5}(s=0)}{B_{\varphi=0}(s=0) + B_{\varphi=\pi/5}(s=0)}. \qquad (2)$$

Figure 2 compares the magnetic field strength along the magnetic axis for each magnetic topology over one period, encapsulating the beam section ($\varphi = 2n\pi/5$ with $n = 0, .., 4$) and the triangular section ($\varphi = (n+1)\pi/5$ with $n = 0, .., 4$).

	MR %	max(B) [T]	min(B) [T]
High	9.4	3.14	2.14
Standard	3.5	2.95	2.22
Low	-0.8	2.92	2.28

Table 1: Comparison of some key values for the different magnetic equilibria investigated in this paper. Note that max(B) and min(B) are the maximum and minimum field values everywhere in the plasma (not at $s = 0$).

Representative parameters of equation 2 for high, low and moderate mirror equilibria are highlighted in table 1. The High Mirror equilibrium is considered to be the best optimised ("advanced") magnetic topology for good reactor performance at high plasma beta, utilising the benefits of the complicated three-dimensional geometry of W7-X. Low mirror is more like a classical stellarator where the magnetic field value along the magnetic axis is nearly constant for all toroidal angles. Stellarators are known for having considerably larger radial diffusion of particles at low collisionality than tokamaks (the so-called 'super-banana' regime [17]). In order to reduce this radial diffusion, the approach taken for the high mirror equilibrium is to create a toroidal magnetic well such that the minimum value of the magnetic field is located in a region where the average magnetic curvature is minimised, i.e. in the triangular section. The majority of the trapped particle population will therefore not be able to access the bean section of the stellarator where the average magnetic curvature and thus the radial diffusion is at its highest.

[1]The free-boundary VMEC equilibria are available with EUROfusion access on the dedicated IPP data server

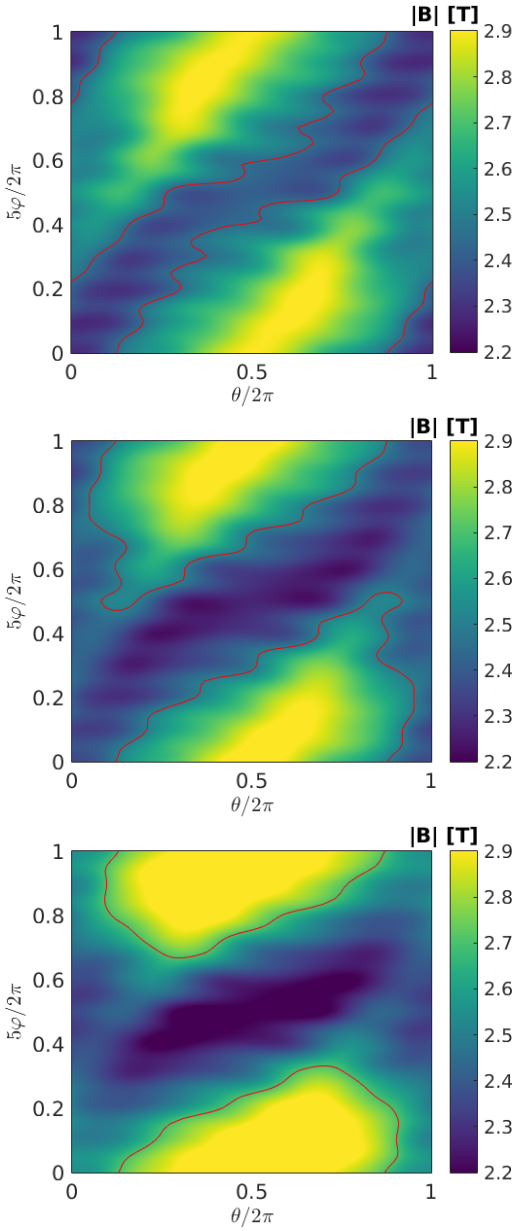

Figure 3: Plot of the magnetic field strength $|B|$ on the flux surface $\rho = \sqrt{\psi_{tor}/\psi_{tor,edge}} = 1.0$ for each of the different equilibria considered in this work: top) Low Mirror, middle) Standard Mirror and bottom) High Mirror, red line indicates the magnetic resonant surface to be described in section 4.

Figure 3 shows angular plots of $|B|$ at $\rho = 0.5$ for each of the three equilibria. Without the presence of Coulomb collisions or neoclassical plasma flows, particles with $B_{ref} = E/\mu < 2.4T$ in the low mirror equilibrium would precess toroidally over long time scales. However, for the High Mirror (bottom) most of these particles would be toroidally trapped and be subject to possible super-banana trajectories. As will be shown in sections 3 and 4, the role of the precession of particles in the toroidal and poloidal direction plays an important role in the confinement of trapped energetic particles in stellarator equilibria.

2.3 Ambipolar Electric Field Inclusion

An ambipolar electric field is established in 3D configurations in order that average currents across flux surfaces vanish. These currents are generated by the differences in the radial transport between ions and electrons, which is smaller for electrons due to their smaller larmor radii. This therefore generates an ambipolar electric field to maintain quasineutrality, improving ion confinement. The magnitude of which is shown in figure 4. This field can be calculated through the following steps (described in [18]). The monoenergetic transport coefficients D_{ij}, as shown in [19], are obtained e.g. with the use of the DKES code [20]. With the inclusion of particle and heat source estimations as well as the ECCD current profile and other factors mentioned in [21], the radial electric field profiles then can be calculated. In order to ensure consistency for each of the three magnetic equilibria investigated in this paper, all of the same parameters and profiles were taken in order to produce the radial electric field profile $E_r(\psi)$. Therefore, only the magnetic topology was a varied parameter for the calculation of $E_r(\psi)$. The resulting fields are shown in figure 4 for each magnetic configuration.

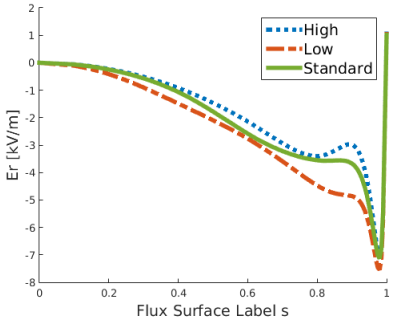

Figure 4: Radial electric field profiles calculated with the different magnetic geometries.

The influence of the ambipolar electric field is to induce both poloidal and toroidal plasma flows. The electric field affects the particle motions through the associated $\boldsymbol{E}\times\boldsymbol{B}$ particle velocity drift, which has components in only the poloidal and toroidal directions (i.e. no component across flux surfaces):

$$\boldsymbol{v}_{\boldsymbol{E}\times\boldsymbol{B}} = \frac{\boldsymbol{E}\times\boldsymbol{b}}{B^*_{\|}} = \frac{E_r}{|\nabla s| B\sqrt{g} B^*_{\|}}(B_\theta \boldsymbol{e}_{\boldsymbol{\varphi}} - B_\varphi \boldsymbol{e}_{\boldsymbol{\theta}}). \quad (3)$$

Where B_θ and B_φ are the contravariant poloidal and toroidal magnetic field components directions respectively, $\boldsymbol{e_\theta}$ and $\boldsymbol{e_\varphi}$ are the unit vectors in the poloidal and toroidal directions respectively, $\sqrt{g}$ is the jacobian, ∇s is the gradient in the radial direction $s = \psi_\varphi/\psi_{\varphi,edge}$ and $B^*_\parallel = \boldsymbol{b} \cdot (\boldsymbol{B} + \rho_\parallel \boldsymbol{\nabla} \times \boldsymbol{B})$ is the modified magnetic field in the parallel direction. The ambipolar electric field has a differing influence on single particle motion in each of the magnetic equilibria, as shown in the example illucidated in figure 5. The particle orbits shown were calculated without the presence of Coulomb collisions for particles with a thermal energy $E = 4keV$ and a pitch angle $\lambda = 0.3$. In the high mirror equilibrium (b) the induced toroidal motion from the electric field does not significantly influence the confinement of the particle, as the strong toroidal magnetic well prevents toroidal period precession. However, in the low mirror equilibrium (a), particle confinement has been improved thanks to the toroidal and poloidal motion generated by E_r.

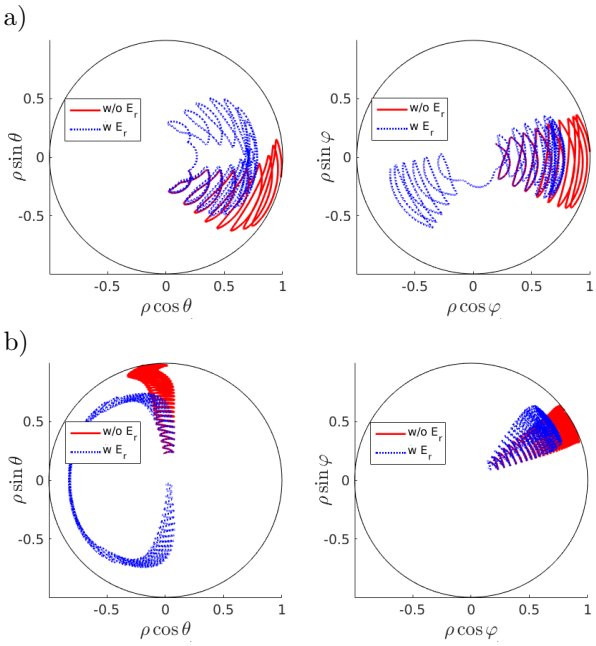

Figure 5: Examples of the contrasting influence of the ambipolar electric field on particle confinements for a) low mirror, b) high mirror. Plotted on the left over the poloidal (pseudo) plane, and the right the toroidal (pseudo) plane.

This high mirror case is consistent with earlier investigations into the influence of the amplitude of the radial electric field using VENUS-LEVIS. In reference [22], the results show that modifying the amplitude of the radial electric field profile by a large factor (1−3 times the original amplitude) does not strongly impact the number of lost particles from the system. The largest difference was found for reasonably energetic particles of 60keV where the effects were still quite small.

3 Neutral Beam Heating Modelling in W7-X

The deposition of the particles injected into a plasma can be calculated by a well known and simple equation for the beam deposition [23],

$$\frac{N_{beam}(l)}{N_{beam,0}} = e^{-\int_0^l n_e(l')\sigma_{eff}(l')dl'}. \quad (4)$$

Where l represents the line entering into the plasma from the NBI beam Positive Ion Neutral Injector (PINI) and σ_{eff} is the total cross section. This is a sum of the reactions that result in the deposition of a neutral particle: charge exchange and ionisation with background electrons and ions (including impurities). Resultingly, the beam deposition depends on the implementation of a realistic NBI geometry for each beam module as well as the plasma parameters such as density along the beam line and the plasma-neutral collision cross section σ_{eff}. In the neutral beam deposition module code VENUS-NBI [11], the collisional cross sections are calculated using the equations proposed in [24]. The equation used to calculate the charge exchange cross section is ~ 10 times larger than ionisation with electrons for W7-X relevant densities and temperatures, given by

$$\sigma_{cx} = 0.6937 \cdot 10^{-18} \frac{(1 - 0.155 \cdot \log_{10} E)^2}{1 + 0.1112 \cdot 10^{-14} E^{3.3}}. \quad (5)$$

The effects of the multistepping correction to σ_{eff} introduced by S. Suzuki, et al (1998) are also included. This is taken as $1.4 \cdot \sigma_{eff}$, corresponding to an electron density of $\sim 10e^{-20}$ and Zeff between $1 - 1.5$. The VENUS-LEVIS NBI module [11] has been recently updated to handle three-dimensional Last Closed Flux Surface (LCFS) geometries when calculating the entry and exit points of the beamline, previously having the capability for only axisymmetric systems. This is performed via the use of the method of volume pixelisation known as 'voxelisation' [25]. To calculate whether a test particle lies within the surface, a cubic grid is produced to encompass the entire structure.

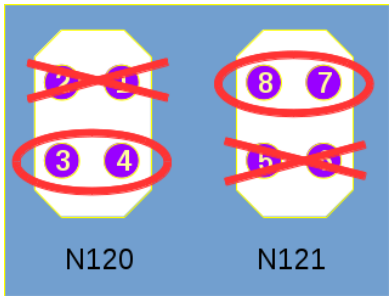

Figure 6: Labelling of the two NBI modules of W7-X, indicating which injectors have been used for the work presented in this paper in accordance with the setup for the first few experimental campaigns.

The injected beam particles are then binned into one of the small cubic elements. The LCFS shape is then discretised into triangular elements, and using basic planar equations between the surfaces of the cube with the surface of the triangles. Using this, an evaluation is made into whether a cube (a group of particles) exists within the plasma. Implementation of this update allows the study of NBI deposition in W7-X with realistic PINI geometry. Currently two NBI modules are installed on W7-X: N120 and N121, each of which house four individual injectors. The location of these modules is as follows N120$(R, Z, \phi) = (6.750, -0.305, 0.993)$ and N121$(R, Z, \phi) = (6.750, 0.305, 1.520)$.

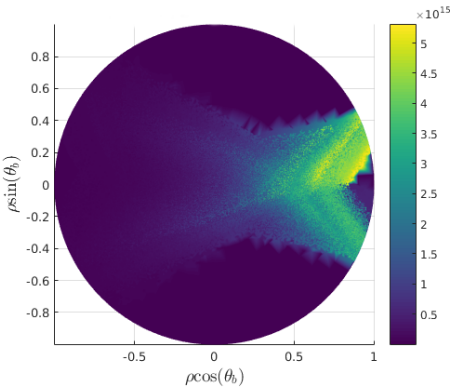

Figure 7: Neutral beam deposition profile for the standard mirror mapped with $\langle\beta\rangle = 3\%$ in a pseudo-cartesian coordinate system distorting flux surfaces into concentric circles for visualisation.

Only two injectors per module have been used in the studies presented here, shown in figure 6, chosen according to what will be used within the first few experimental campaigns on W7-X. There are two slightly more tangential injectors, 4 and 8, at 1.78MW and two slightly more normal injectors, 3 and 7, at 1.64MW. The species power fraction for the hydrogen beam was set to 54.6%, 30.9% and 14.5% for the H, 2H and 3H neutral molecules respectively. The results were benchmarked successfully with other beam deposition codes such as BBNBI [26], NUBeam [27] and Beams3D [28].

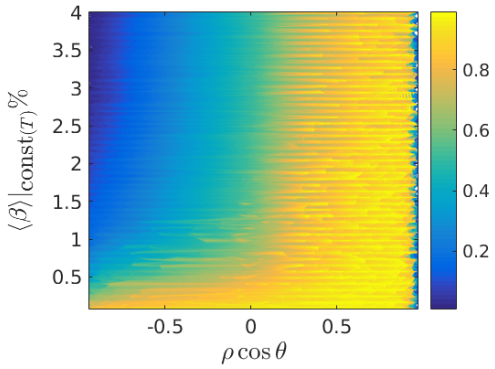

Figure 8: Normalised radial neutral beam deposition profile for the high mirror as a scan in the normalised plasma beta value <β> (for constant temperature and varying density profiles).

The use of the same density and temperature profiles for each magnetic equilibrium leads to similar neutral beam deposition profiles. Figure 7 illustrates the obvious problem with NBI as an auxiliary heating source for high beta 'flat-top' density profile plasmas, i.e. that the particle ionisation occurs at the edge, a result also found in [3]. For reasonable core penetration of NBI ions, while maintaining the temperature, the density would have to be reduced to such an extent that $\langle\beta\rangle$ would be reduced to $\langle\beta\rangle > \sim 0.2\%$. This is reflected in figure 8. In contrast, W7-X has been optimised for $\langle\beta\rangle \sim 5\%$. Good performance of a neutral beam heating system depends on the confinement of the beam ions and whether a substantial amount of energy of the beam ions can be transferred efficiently to the background plasma before the particle is lost from the system. As mentioned in the introduction, detailed work on the loss and diffusion of neutral beam particles has already been studied in references [3] and [4]. Further work will be presented here to make a comparison between the different magnetic topologies and also for a later comparison between Ion Cyclotron Resonance Heating and NBI heating. By utilising the guiding-centre following code VENUS-LEVIS [13], two different methods to simulate NBI particle behaviour have been investigated. In section 3.1 all markers are injected into the system at t=0, and are followed in order to investigate the confinement properties in the different magnetic topologies. In section 3.2, particles are constantly injected throughout the entire simulation in order to develop a realistic slowing down particle distribution.

3.1 Losses and Diffusion

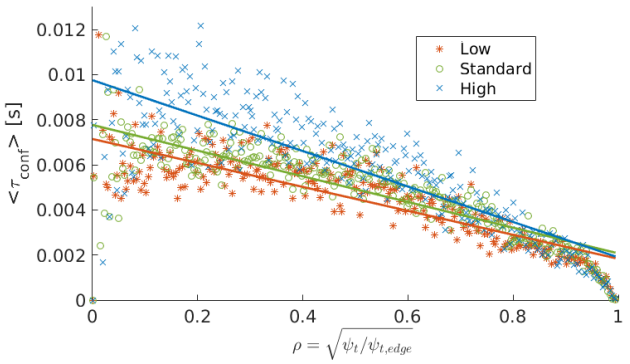

Figure 9: The confinement time of the particles plotted against the initial radial position, taken as the average of all the markers discretised in ρ, the radial flux surface label. Also plotted are linear fits to the data.

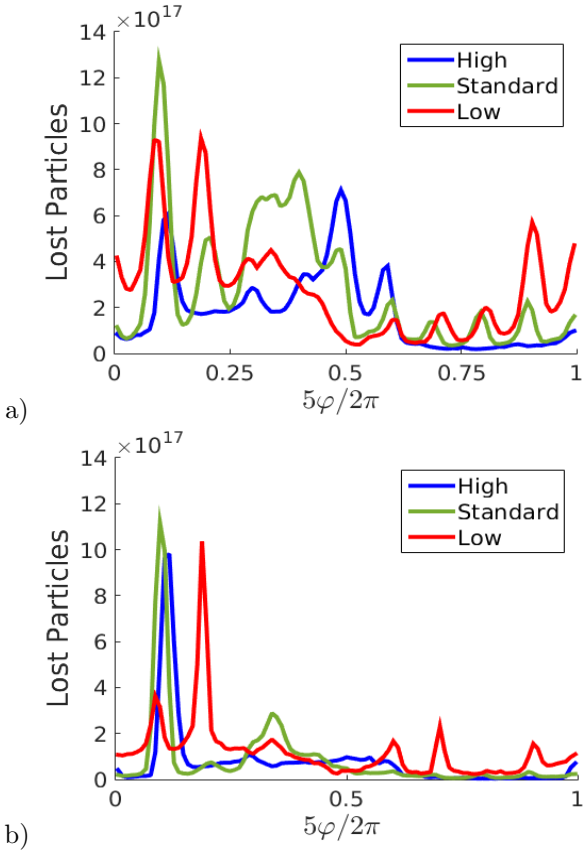

Figure 10: Neutral beam injected particle losses as a function of the toroidal angle, summated over all toroidal periods a) with and b) without Coulomb Collisions.

The losses and radial diffusion of neutral beam particles can be investigated by recording the initial position of a particle and the position and time at which it reaches the last closed flux surface. This information enables calculation of the improved confinement time of NBI particles in the high mirror equilibrium relative to the low mirror case, as shown in figure 9. Evaluating the density of lost particles as a function of the toroidal position, shown in figure 10, this indicates the different loss mechanisms present in each case. The x-axis has been normalised to extend over one toroidal field period. Noting that the summation of losses over all toroidal periods also contains local effects such as first and multiple orbit losses, which only arise in specific toroidal locations. Figure 10 (b) represents the same simulations but without the presence of coulomb collisions. By comparison of figure 10 (a) and (b), it is seen that collisions act to 'kick' and therefore spread the particles to have less distinct loss regions. This behaviour arises via pitch angle scattering in the Monte-Carlo Coulomb collision operator, which is modelled in the VENUS-LEVIS [13] code. A comparison of figure 10 (a) and (b) illustrates that collisionality enhances particle losses as is known from neoclassical transport for stellarators [29, 30]. For the low mirror configuration there are substantial losses at all toroidal locations, and for the high mirror the losses tend to be concentrated around the triangular sections of the stellarator.

In the collisionless simulations of figure 10b), the standard mirror appears to have two distinct angles, $\varphi/10\pi \sim 0.12, 0.35$, where significant losses occur, most occuring at $\varphi/10\pi \sim 0.12$. With the inclusion of coulomb collisions (figure 10a)), the relative magnitudes of these two dominant toroidal loss channels becomes comparable. Similar characteristics can be found in the high mirror equilibrium. However, in the low mirror equilibrium the largest fundamental loss channel remains predominant, and an explanation of other loss regions is not evident from a comparison with the simulation without the presence of Coulomb collisions.

3.2 Slowing Down Distribution Function

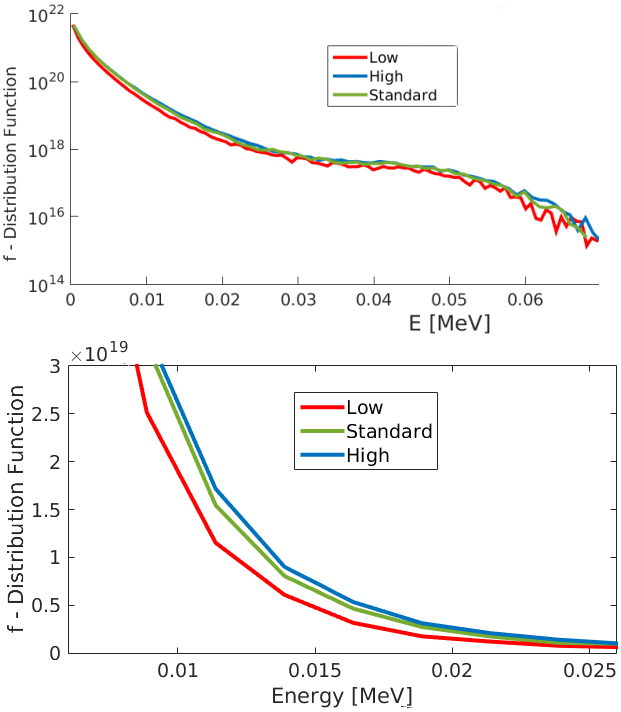

Figure 11: Slowing down beam energy distribution function for all NBI particles in linear-log space with a zoom into the energy region 6-25keV (linear-linear).

Taking the neutral beam deposition particle profile generated in section 3 and constantly injecting the markers throughout the simulation provides a prediction of the performance of NBI in experimental scenarios. A measure of this performance is the energy distribution of the beam ion population respectively via the length of the tail and the power transferred to the background species. The three magnetic configurations are compared in figure 11a). Despite the improved particle confinement time of the high mirror in comparison with the other magnetic topologies, the slowing down energy distribution functions are not drastically dissimilar. Nevertheless, removing the log scale for the y axes shows that for $E = 20$keV the high mirror confines almost twice the number of particles than the low mirror equilibrium, (see figure 11(b)). A reasonably substantial population of beam particles with $E \lesssim 50keV$ is maintained in the system for all magnetic equilibria., but at higher energies the ambipolar electric field does not assist particle confinement.

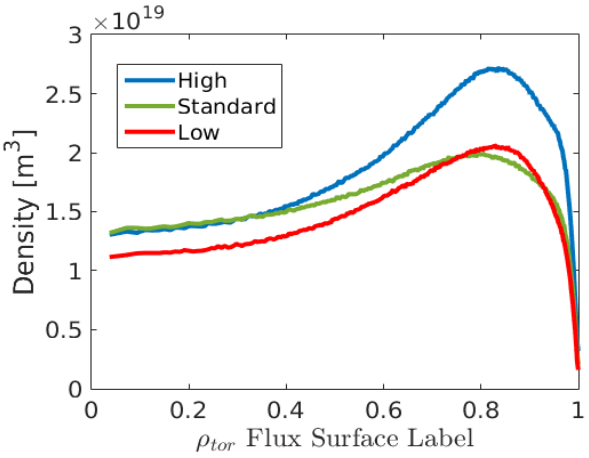

Figure 12: Edge localisation of the NBI particles, taken from the slowing down distribution.

While it is found that beam ions are confined up to reasonably high energies, the crucial issue is the edge localisation of the initial particle deposition. Continuous injection and collisions produce a slowing down distribution which remains peaked at the edge of the plasma, as indicated by the density, shown in figure 12. The edge localisation of the beam particles poses a serious difficulty for the success of the NBI heating method, and therefore on the ability of W7-X to demonstrate relevant conditions to produce large numbers of fusion reactions.

3.3 Summary of NBI Heating

The neutral beam ionisation code VENUS-NBI [11] has been updated to calculate the beam deposition in three dimensional geometries using the method of Voxelisation. Including the realistic geometry of the NBI injector geometry of W7-X allows the simulation of the fast ions injected into the system. Modifying the background plasma density, it has been shown that poor beam penetration to the plasma core is expected until the confinement becomes deoptimised (due to low $\langle\beta\rangle$ values), irrespective of the toroidal magnetic mirror value. Particles are ionised at the plasma edge, and even after slowing down timescales the particles are either lost or remain strongly edge localised. Evidence to explain the differences in performance of NBI in the different equilibria is found through studies of the lost particle populations. By considering the initial and final position of all the lost particles, it has been shown that the high mirror equilibrium has the largest average confinement time for all radial positions, followed by the standard mirror. The low mirror equilibrium has the largest radial diffusion and resultant losses. Simulating the beam ion motion with and without the influence of

Coulomb collisions reveals the presence of different magnetic loss channels, which are specific to each magnetic mirror equilibrium. The loss channels remain distinct in the low mirror even when collisions are induced.

4 Ion Cyclotron Resonance Heating

Two ICRF antenna's are foreseen to be installed on the W7-X stellarator [31]. The first to be commissioned consists of two straps with a total power output of 1.5MW. The operational frequency range is 25-38MHz which permits on-axis fundamental heating of both hydrogen and helium-3 for plasmas with $B_0 \simeq 2.5T$. Simulations relevant to this antenna for various heating schemes will help to focus experiments, especially with regard to optimal magnetic configurations.

The strength of the ICRF wave-particle interaction strongly depends on two factors: the polarisation and the refractive index of the wave at the point of resonance. Neglecting the RF-perturbed magnetic field (and therefore Transit Time Magnetic Pumping (TTMP) effects), and knowing that relevant ICRH scenarios always have $\omega_{p,\alpha}^2 >> \omega^2$, the refractive index can be written as,

$$n_\perp^2 \simeq \frac{(R - n_\parallel^2)(L - n_\parallel^2)}{S - n_\parallel^2}. \tag{6}$$

In the cold plasma assumption approximate forms of R, L and S can be calculated directly,

$$R \simeq 1 - \sum_\alpha \frac{1}{\omega} \frac{\omega_{p,\alpha}^2}{\Omega_\alpha + \omega}, \tag{7}$$

$$L \simeq 1 + \sum_\alpha \frac{1}{\omega} \frac{\omega_{p,\alpha}^2}{\Omega_\alpha - \omega}, \tag{8}$$

$$S \simeq 1 + \sum_\alpha \frac{\omega_{p,\alpha}^2}{\Omega_\alpha^2 - \omega^2}. \tag{9}$$

Reflection of the wave occurs when $n_\perp \to 0$, which is determined by the parameters R and L. The variable S determines the region of energy exchange between the wave and particle since absorption reverses this: $n_\perp^2 < 0$. Polarisation refers to the relative strength of the electric field rotating in the direction of the ions compared to that of the electrons,

$$\left|\frac{E_+}{E_-}\right|^2 \simeq \left(\frac{R - n_\parallel^2}{L - n_\parallel^2}\right)^2, \tag{10}$$

where,

$$E_+ = E_x - iE_y,$$
$$E_- = E_x + iE_y.$$

The role of R and L in equation 10 ensures that the polarisation of the wave depends not only on the charge to mass ratios of each species in the plasma, but also on the relative concentration of each species through the plasma frequency $\omega_{p,\alpha}$. Consideration of the two key parameters, R and L, have assisted the development of the characterisation of many different heating schemes described further in section 4.2.

4.1 Resonant Surfaces

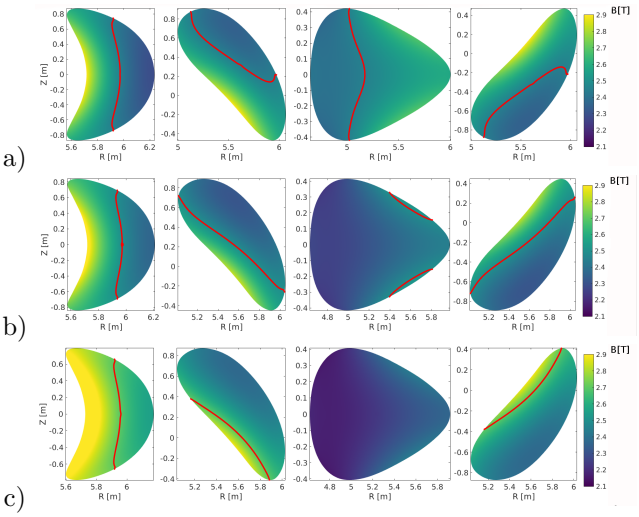

Figure 13: The magnetic field strength contours at the toroidal locations $\varphi = 0, 3\pi/10, 1\pi/5$ and $3\pi/5$ (from left to right) for the three different equilibria: a) Low, $B_c = 2.45T$, b) Standard, $B_c = 2.5T$ and c) High, $B_c = 2.7T$. The red line indicates the resonant magnetic field value B_c for on-axis heating at the toroidal antenna position 6.7°.

The interaction between the ICRF-wave and a particle occurs when the following resonance condition is satisfied,

$$\omega = k_\parallel v_\parallel + n\Omega_{c,i}, \tag{11}$$
$$\Omega_{c,i} = \frac{Z_i e B}{m_i}.$$

n being the harmonic number of the cyclotron frequency, as a result of Finite Larmor Radius (FLR) heating effects. In the work presented here, only fundamental ($n = 1$) heating will be studied. Concerning equation 11, this implies that wave-particle energy exchange occurs along constant magnetic field contours. This absorption region is then broadened via a Doppler-shift-like effect, present in the first term on the right hand

side of equation 11. The RF antenna frequency is constant such that the resonant interaction occurs on the magnetic axis at the same toroidal location as the ICRF antenna. For different toroidal positions, figure 13 illustrates the regions where particles receive energy from the wave: near to the red lines. The influence of the equilibrium toroidal magnetic mirror on the displacement of the resonance location. For the high mirror equilibrium, there are no possible means of efficient energy transfer near to the triangular toroidal section ($\varphi = 1\pi/5$). In contrast to this, the low mirror equilibrium permits strong on-axis resonance for all toroidal locations around the stellarator.

4.2 ICRF Heating Methods

One of the most commonly used ICRF heating methods is referred to as the 'minority species heating scheme', where a small concentration (roughly between 1-5%) of a minority species is added to the plasma. In terms of the refractive index, the absorption region of $n_\perp^2 < 0$ occurs somewhere between the limiting cyclotron frequencies $\Omega_{c,maj}$ and $\Omega_{c,min}$. This region is known as the ion-ion hybrid resonance layer. For small concentrations of the minority species an upper limit on the wave polarisation can be found as

$$\max \left| \frac{E_+}{E_-} \right|^2 \simeq \left(\frac{\Omega_{c,maj} - \Omega_{c,min}}{\Omega_{c,maj} + \Omega_{c,min}} \right)^2 . \qquad (12)$$

The advanced ICRF '3-ion species' heating scheme requires a plasma composed of two different majority species, and extremely small concentrations of a third minority species. Similarly to the minority species scheme, wave-particle resonance $n_\perp^2 < 0$ occurs in a region dictated by the charge mass ratio of the three species as well as the relative species concentrations. If the condition

$$(Z/A)_{M(1)} < (Z/A)_{min} < (Z/A)_{M(2)}. \qquad (13)$$

is satisfied, then this resonance region is closely located to the 'L' cutoff layer, where

$$\left| \frac{E_+}{E_-} \right|^2 >> 1. \qquad (14)$$

The polarisation is maximised in the absorption region if the concentration of the minority species is sufficiently low, permitting efficient ICRF-particle coupling. In this paper, a focus is made on the 3-ion species scheme performance, using the plasma concentrations X[H]=68%, X[4He]=15.9% and X[3He]=0.1%. Furthermore, a comparison is made with the standard minority heating scheme, investigating the performance of a minority concentration of X[H]=2% in a Helium-4 plasma background. The choice of this plasma species mixture is given by equation 8 in reference [6],

$$f^*_{M_1} \simeq \frac{\tilde{Z}_{min} - \tilde{Z}_{M_1}}{\tilde{Z}_{M_2} - \tilde{Z}_{M_1}} - \frac{(\tilde{Z}_{M_2} - \tilde{Z}_{min})(\tilde{Z}_{min} - \tilde{Z}_{M_1})}{\tilde{Z}_{M_2} - \tilde{Z}_{M_1}} \zeta, \qquad (15)$$

where $\tilde{Z}_\alpha$ is the charge to mass ratio $(Z/A)_\alpha$ and ζ is related to plasma parameters such as the electron density, major radius and parallel wave number of the injected ICRH.

4.3 Fast Ion Pressure Distribution

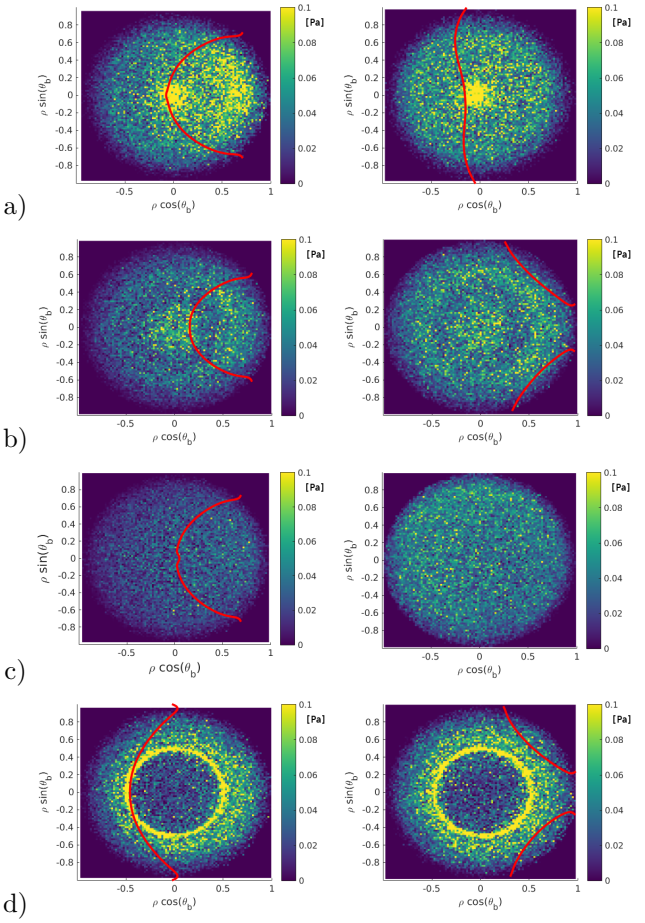

Figure 14: Fast ion ($v > 5v_{th}$) pressure plots for a) low, b) standard, c) high and d) HFS heating in the low mirror equilibria for the 3-ion species ICRH scheme. Left) Bean section $\varphi = 0$, right) triangular section $\varphi = \pi/5$. The red line indicates the line of resonance according to the B_{res} contour.

The relative performance of ICRH for each equilibrium can be seen through the comparison of the development of large fast ion pressures, shown over the bean

and triangular (pseudo) poloidal planes in figure 14. The separation of fast and thermalised particles was undertaken through a condition on the local (to the flux surface) thermal velocity $v > 5v_{th}$ at any given position in configuration space. Immediately noticable is that the low mirror equilibrium generates considerably larger fast ion pressures than both the standard and high mirror cases. In addition to this, the pressure peaking on-axis is maintained even in the triangular toroidal section, away from the ICRF antenna. Pressure peaking associated with trapped particles can be seen in the bean section toroidal image (left) of the low mirror, since trapped particles align their bounce-tips with the resonant layer, a point further explained in section 4.4. Particularly interesting is that the fast-ion pressure peaks in the triangular toroidal section, rather than in the bean section where the RF-antenna is located. This is as a result of the toroidal particle trapping mechanism. The particles are heated in the perpendicular direction and the orbits then transition to become deeply trapped in the toroidal well between two bean periods.

4.4 ICRH-Modified Radial Diffusion

The Quasi-Linear Operator of VENUS-LEVIS [13] employed to simulate wave-particle interaction through a Monte-Carlo process utilises the perpendicular velocity diffusion coefficient,

$$Q_\perp = \frac{\pi Z_\alpha^2}{2m_\alpha^2}|E_+ J_{n-1}(\epsilon) + E_- J_{n+1}(\epsilon)|^2 \delta(\omega - k_\parallel v_\parallel - n\Omega_c), \tag{16}$$

with $\epsilon = k_\perp v_\perp / \Omega_{c,\alpha}$ associated with the influence of Finite Larmor Radius (FLR) effects. This leads to an equation for the wave-particle 'kick' in the perpendicular direction. The Kennel-Engelmann constraint can then be applied to calculate the associated parallel wave-particle interaction.

$$v_\perp^2 + \left(v_\parallel - \frac{\omega}{k_\parallel}\right)^2 = const. \tag{17}$$

As described by T. Stix [1], this constraint naturally incorporates the physics that particles will align their bounce tips with the ICRF-resonant surface, a phenomena that applies to both tokamak and stellarator configurations.

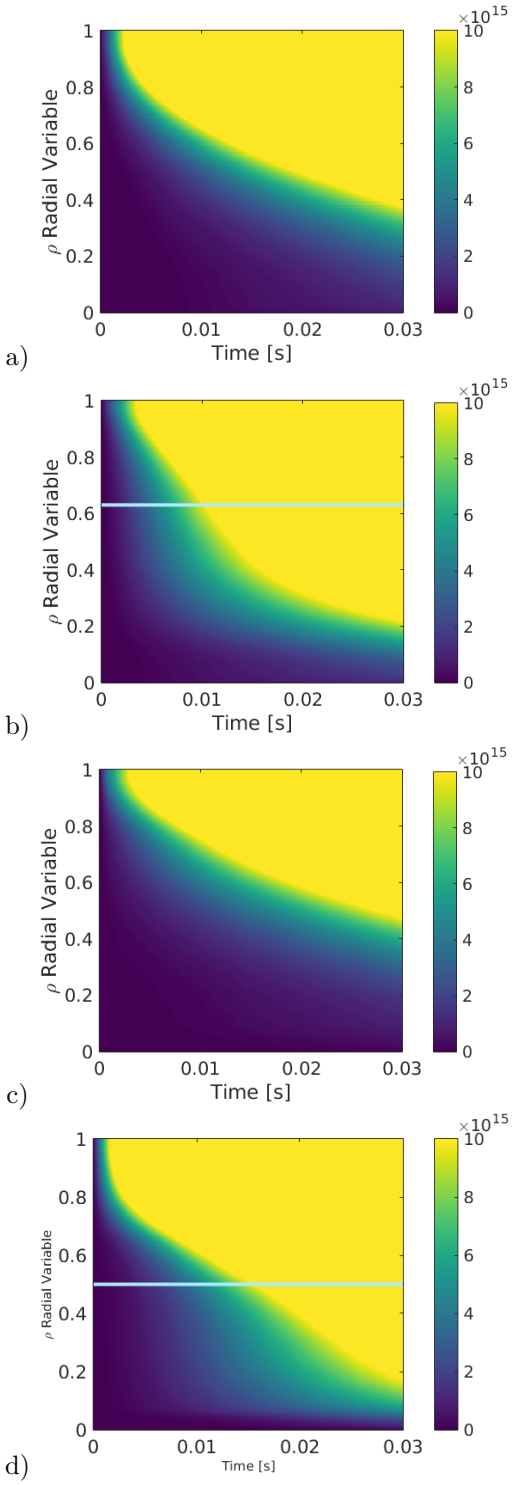

Figure 15: Lost particle contour plots for the ICRH simulations with respect to the initial radial position in ρ and the time when the particle is lost, for a) Low, b) Standard, c) High and d) Low (HFS heating) mirror equilibria. The light blue line corresponds to the position of the radial peaking of the fast ion pressure visible in figure 14

Investigating the influence of the resonant surface on the alignment of particle bounce tips, this section will focus on the radial particle diffusion and the associated losses. The total particle losses were 12.0, 14.8 and 13.3% in the high, standard and low mirror configurations respectively. In the high mirror, particles do not interact significantly with the resonant surface. Once they interact with the RF-wave, they become trapped and move into the large toroidal magnetic well specific to this equilibrium. The region of largest electric field amplitude is located close to the RF-antenna, which lies near the bean shape. Therefore, particles cannot easily remain in resonance with the wave before becoming trapped in regions of lower field amplitude. Evidence for this is reflected in the pressure peaking shown in figure 14 c), which indicates that the average pressure is highest in the triangular section, away from the RF-antenna. This phenomena is also observed in the standard mirror, shown in figure 14 b). However, the weaker toroidal magnetic mirror of the standard mirror still permits the toroidally trapped resonant particles to access regions of larger electric field amplitude near to the RF-antenna. This results in the overall larger fast ion pressure observed in the standard mirror. Despite this, the standard mirror has the largest percentage particle losses. NBI studies shown in section 3.2 can provide evidence for this increase in lost particles. Figure 12 illustrates the radial density profile resulting from the NBI heating. In the core region $\rho < 0.35$ the good particle confinement is similar to that of the high mirror. However, for $\rho > 0.75$ this confinement is degraded and becomes the worst performing configuration of the three. In the case of ICRH in the standard mirror, the toroidal displacement of the RF resonant surface away from the core region acts to move particles away from this region of improved confinement. Entering the edge region of worse confinement, resonant particles are then lost from the equilibrium. Further evidence for this is shown in figure 15 b). The light-blue line at $\rho \sim 0.64$ indicates the observed edge pressure peaking shown in figure 14 b). Particles within this surface have a large outward radial diffusion, whereas close to or just outside of this surface the diffusion is reduced. The low mirror configuration has lower percentage particle losses than the standard mirror. Resonant particles in the core tend to align their bounce tips close to the axis, leading to improved particle confinement. To further investigate the radial diffusion in the presence of ICRH, a simulation of off-axis (High Field Side - HFS) heating in the low mirror configuration with $B_c = 2.6T$ is shown in figure 15 d). The radial location where the particles tend to most strongly interact with the wave results in a pressure peaking of resonant particles with a reduced radial diffusion. This is further reflected in the off-axis pressure peaking at the resonant surface in the bean section shown in figure 14 d) (left). The off-axis low mirror simulation resulted in a total percentage loss of 18.7%, considerably larger than on-axis simulations for all other equilibria. Compared to the other simulations of the high, standard and low mirror of on-axis (in front of the antenna) heating, off-axis ICRH in the low mirror produces the largest radial diffusion from the core region, degrading the performance of the low mirror. The antenna frequency and therefore location of the RF-resonant surface is concluded to have a large influence on the radial diffusion of resonant particles.

4.5 ICRH Distribution Functions

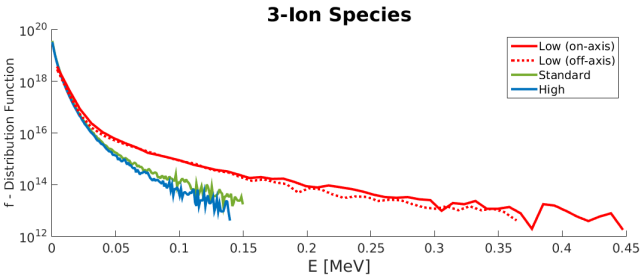

Figure 16: Comparison of the resultant distribution functions of the 3-ion species heating scheme for the different magnetic equilibria, including the off-axis low mirror simulation.

The resulting fast ion distribution functions for the advanced 3-ion species RF heating scheme are shown in figure 16. Unlike the NBI slowing down distribution functions, it is evident that the performance of ICRH is significantly influenced by the toroidal magnetic mirror amplitude. Simulations of both on and off-axis heating in the low mirror equilibrium reflect the improved performance of the low mirror equilibrium, in particular for generating highly energetic ion populations, despite the lower confinement time of NBI fast ions (figure 9). Comparing the high and standard mirror, the standard mirror succeeds in producing more highly energetic ions above the energy $E > 0.05MeV$, despite the increase in lost particles.

4.6 Summary of ICRF Heating

The propagation of ICRF waves in 3D magnetic geometries was presented in section 4.1, illustrating the influence of the toroidal magnetic mirror effect on the displacement of the RF resonant surface. Additionally, with respect to the RF-antenna to be installed on W7-X in Spring 2018, the main ICRF heating schemes applicable are the minority species and the 3-ion species heat-

ing schemes, explained in section 4.2. Focusing on the latter heating scenario, the results explain the influence of the presence of the ICRF resonant surface on confinement. The influence of ICRH to align the bounce tips of a particle with the resonant surface can have either a positive or a negative impact on the overall performance, due to the intricacies of the three-dimensional magnetic equilibrium used. For the standard mirror case, as shown in figure 13, the line of resonance is radially displaced from the magnetic axis. When the particles align their bounce tips with this layer they are then radially displaced outwards into regions of reduced confinement. However, the increase in radial diffusion does not necessarily result in a reduced fast ion pressure or energetic distribution function. Illustrated in figures 16 and 14, the off-axis low mirror configuration also generates highly energetic particle populations and fast ion pressures. This is because the reduced displacement of the resonant surface - compared to the standard or high mirror - allows particles to remain in resonance, thus increase in energy, despite the larger total losses. The highly energetic particles produced by the 3-ion species scheme in the low mirror equilibrium could be used in experiments to replicate the behaviour and confinement of alpha particles, and to provide an insight into particle-Alfvén Eigenmode resonant interaction in W7-X.

5 Comparison of Heating Schemes

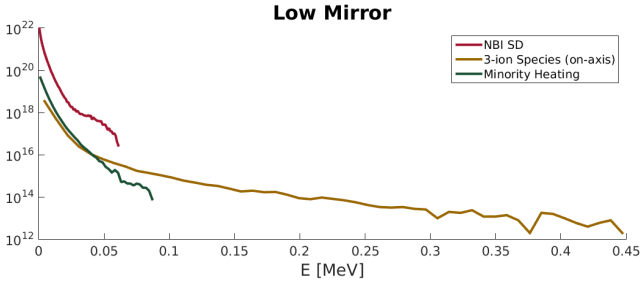

a)

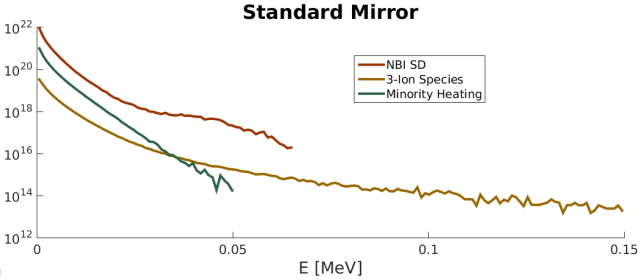

b)

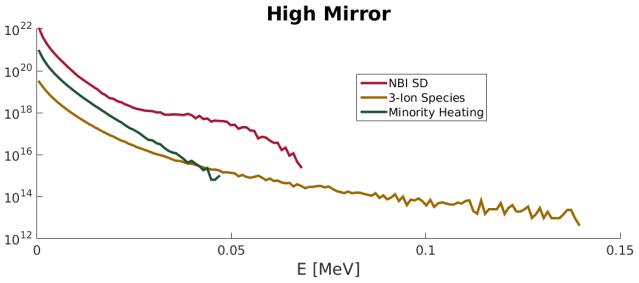

c)

Figure 17: Comparison of the resultant distribution functions from NBI and ICRF heating, where both the ICRF minority heating and 3-ion species heating schemes have been included for the a) low , b) standard and c) high mirror equilibria. Noting different x-axis used for the low mirror case.

The resulting fast ion distribution functions for each of the heating schemes are presented in figure 17, including that of the minority species heating scheme described briefly in section 4.2. With respect to the development of a large concentration of fast particles, the relative differences in the distribution functions for large energies is smaller for NBI heating when comparing all magnetic equilibria. Regarding the population of highly energetic fast ions, the three ion species outperforms the other heating schemes, especially for the low mirror magnetic geometry. Comparing the distribution functions of figure 17 provides an understanding of the confinement of energetic ion particles in the different magnetic equilibria. In contrast, the heating transferred to the background plasma is reflected in the collisional and lost power. Tables 2 and 3 reflect the balance of the input-power (for NBI and 3-ion species ICRH respectively) with the two output power channels: the lost and collisional power. These two tables were calculated differently. For NBI heating, the two output powers were evaluated using all of the losses and collisions throughout the entire simulation. For ICRF heating, a state of saturation in energy is first achieved and then the lost and collisional power is evaluated with the data obtained upon convergence. Note that the powers do not balance for NBI simulations due to the energy stored in the distribution function.

Mirror	$P_{in}[MW]$	$P_{cols}[MW]$	$P_{lost}[MW]$
High	6.84	4.687	0.804
Standard	6.84	4.189	1.378
Low	6.84	4.173	1.406

Table 2: Details of the total power transfer for the NBI heating scheme.

Mirror	$P_{in}[MW]$	$P_{cols}[MW]$	$P_{lost}[MW]$
High	1.5	1.401	0.099
Standard	1.5	1.346	0.154
Low (on-axis)	1.5	1.228	0.272
Low (off-axis)	1.5	1.186	0.314

Table 3: Details of the converged power transfer for the 3-ion species ICRF heating scheme.

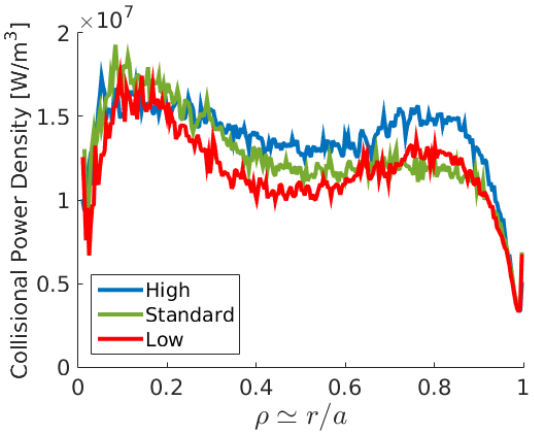

a)

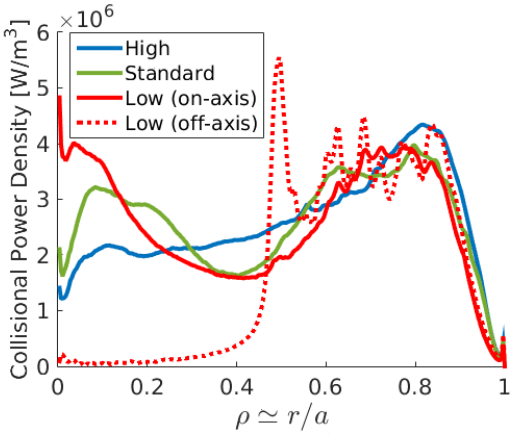

b)

Figure 18: Radial profiles of the fast ion collisional power transfer for: a) NBI and b) ICRF 3-ion species heating.

Analysis of the lost power is calculated through summating the product of the energy and weight over the lost particle population. Therefore, it provides insight into both the confinement of the particles and the lost energy. The collisional power directly implies the heating transferred to the background plasma. For NBI heating, the collisional and lost power balance shown in table 2 reflects that the differences between the low and standard mirror are not significantly large when compared to the high mirror. Furthermore, analysis of the lost power implies the improved performance of the high mirror in the overall confinement of the beam particles. Table 3 illustrates that, despite producing highly energetic fast ion populations, the low mirror equilibrium does not transfer as much power to the background population as for the case for the high and standard mirror configurations. The small increase in lost power is due to the poor confinement of energetic particles in this low toroidal mirror magnetic geometry. However, a crucial advantage of the low mirror configuration is the resultant core heating, reflected in figure 18b). Indeed, the radial profiles of the ICRF heating show that localised core heating is only achieved through ICRH in the low mirror. Figure 18a) shows that NBI heating results in reasonable core heating for all equilibria. The standard mirror produces weakly peaked core heating with the 3-ion species scheme, however, due to the strong toroidal dependence of the magnetic resonant surface, there is also significant edge heating. ICRF heating in the high mirror results in strongly off-axis heating at the plasma edge.

6 Summary and conclusions

This work presents the results of the simulated performance of Neutral Beam Injection and Ion Cyclotron Range of Frequency heating in different W7-X magnetic topologies. The three magnetic equilibria have different degrees of toroidal mirroring. The magnetic configurations are optimised for different properties. The high mirror is predicted to be the best performing candidate for high plasma $\langle\beta\rangle$. The standard mirror is foreseen to be the standard workhorse equilibrium used in experiments. Finally, the low mirror is an equilibrium which closely resembles the design of a classical stellarator, with the axial magnetic field strength approximately constant for all toroidal angles.

The VENUS-NBI [32] module has been updated in order to permit the calculation of neutral beam deposition in three-dimensional equilibria, and includes a realistic implementation of the W7-X NBI PINI geometry. The results show that regardless of the magnetic equilibria used, there is poor penetration of the beam into the core of the plasma for reasonable normalised plasma $\langle\beta\rangle$ values. In terms of the confinement and radial diffusion of NBI ions, the particle following VENUS-LEVIS code [13] predicts that the high mirror equilibrium has the largest particle confinement time, especially those ions located near the core. The low mirror is the worst performing magnetic topology for NBI, with the per-

formance of the standard mirror in between high and low mirror equilibria. The final results of the NBI simulations show that the initially edge localised particles remain localised at the edge even for the full slowing down NBI distribution. This result is of considerable concern for the performance of such an auxiliary heating system.

Through the use of the SCENIC code package [9], Ion Cyclotron Resonance Heating simulations were undertaken using an antenna description radially, poloidally and toroidally localised in one of the five W7-X toroidal periods. Particular focus was given to the high-performance 3-ion species ICRF heating scheme. This requires a tailoring of the percentage concentrations of three different plasmas species with specific charge-to-mass ratios. Based on a careful choice of the particle concentrations, this heating scheme permits strong polarisation of the wave close to the wave-particle resonant surface. The predicted fast ion pressure has the largest on-axis amplitude in the low mirror equilibrium. This is due to particles remaining in resonance close to the magnetic axis for all toroidal angles. The high mirror configuration results in the lowest fast ion pressure, due to the resonant surface leaving the plasma before reaching the triangular toroidal section. These lost particles do not result in a large lost power compared to the low mirror equilibrium because the particles do not remain in resonance, and so lost particles have considerably lower energy values. The largest lost particle population produced through on-axis ICRH is in the standard mirror configuration. Similar to the high mirror configuration, the toroidal displacement of the resonant surface acts to increase the particle radial diffusion. This acts to move particles into regions away from the core, resulting in confinement degradation. Due to the reduced toroidal mirror compared to the high mirror configuration, resonant particles in the standard mirror can remain in resonance, despite the toroidal displacement of the resonant surface. This produces an increase in lost power, as the ion energies are larger and the edge confinement is worse than in the high mirror configuration. For on-axis heating, the resonant surface in the low mirror equilibrium does not displace far from the axis for different toroidal angles. This leads to improved on-axis peaking of the fast ion pressure and collisional power density compared to the standard and high mirror configurations. The low mirror configuration also produced the most energetic ion populations, with energies of up to 0.45MeV. The confinement of trapped energetic particles is generally poor in three-dimensional stellarator geometry. Compared to the standard mirror, the low mirror results in fewer particle losses, but a larger lost power. This is a result of the improved confinement in the core due to the location of the resonant surface, but the particles that are lost have higher energies. This poor confinement of the energetic particles results in a lower transfer of power to the background plasma than the other equilibria. Simulating off-axis high field side ICRH in the low mirror configuration provided insight into particle confinement in the prescence of ICRH. It was seen that the fast ($v > 5v_{th}$) ion pressure is peaked over a narrow radial region $0.49 < \rho < 0.51$. This indicates the influence of ICRH on the radial diffusion of resonant particles.

A comparison between the slowing down NBI fast ion distribution with those of the ICRF 3-ion species and minority heating schemes was made in section 5. The three heating schemes have different merits. NBI produces large concentrations of fast ions, yet the resultant particle density profiles are strongly edge localised. This occurs for all magnetic equilibria. In contrast, the 3-ion species ICRH scheme is very sensitive to the magnetic topology, and due to the very small concentrations of the resonant minority species, the fast ion pressure produced is much lower than that produced with NBI heating. The radial profiles of the collisional power indicate that core localised heating can be produced by both NBI and ICRF heating, but the profiles are sensitive to the toroidal magnetic mirroring, moreso with ICRH. Future investigations will be made into potentially combining the 3-ion species scheme with NBI heating via synergetic heating, whereby the third species would be the beam population [33]. This could also be a potential solution for strong core-localised heating performance for both the standard and high mirror equilibria.

Acknowledgments

This work has been carried out within the framework of the EUROfusion Consortium and has received funding from the Euratom research and training programme 2014-2018 under grant agreement No 633053. The views and opinions expressed herein do not necessarily reflect those of the European Commission. The project was also supported in part by the Swiss National Science Foundation. The authors would like to thank Dirk Van Eester and Yevgen Kazakov for their advice and for all the fruitful discussions. The simulations made for this research used both the Piz Daint (CSCS, Switzerland) and the MARCONI-Fusion (CINECA/ENEA, Italy) supercomputer facilities. Additionally, acknowledgements should be made to the SCientific IT and Application Support (SCITAS) centre based at EPFL for help with on-site computer support.

References

[1] Thomas H Stix. *Waves in plasmas*. Springer Science & Business Media, 1992.

[2] T. Andreeva et al. *Prob. of Atom. Sci. Cent.*, 4:R45–R47, 2002.

[3] M. Drevlak et al. *Nuc. Fus.*, 54(073002), 2014.

[4] J.M. Faustin et al. *Nuc. Fus.*, 56(9):092006, 2016.

[5] J. M. Faustin et al. *Plas. Phys. Cont. Fus.*, 58(7):074004, 2016.

[6] Y. O. Kazakov et al. *Nuc. Fus.*, 55:032001, 2015.

[7] Y. O. Kazakov et al. *Nat. Phys.*, 13:973–978, 2017.

[8] J. M. Faustin et al. *Plas. Phys. Contr. Fusion*, 59:084001, 2017.

[9] M. Jucker et al. *Comp. Phys. Comm.*, 182(912-925), 2011.

[10] W.A. Cooper et al. *Comp. Phys. Comm.*, 180(9):1524–1533, 2009.

[11] M. Albergante. *Interaction between fast ions and microturbulence in thermonuclear devices*. PhD thesis, École Polytechnique Fédérale de Lausanne, 2011.

[12] N. Mellet et al. *Comp. Phys. Comm.*, 182:570, 2011.

[13] D. Pfefferlé et al. *Comp. Phys. Comms.*, 185(12):3127 – 3140, 2014.

[14] M. Greenwald. *Plasm. Phys. Cont. Fus.*, 44:R27–R80, 2002.

[15] H.S. Bosch et al. *Contrib. Plas. Phys.*, 50(8), 2010.

[16] S. P. Hirschman et al. *Plas. Fluids*, 26(12):3553, 1983.

[17] P. Helander et al. *Plas. Phys. Cont. Fus.*, 54(124009), 2012.

[18] Y. Turkin et al. *Phys. Plas.*, 18:022505, 2011.

[19] C.D. Beidler et al. *Nuc. Fus.*, 51(7):076001, 2011.

[20] S.P. Hirshman et al. *Phys. Fluids*, 29(9):2951–2959, 1986.

[21] Y. Turkin et al. *Fus. Sci Tech.*, 50(3):387–394, 2006.

[22] J. Faustin. *Self-Consistent Interaction of Fast Particles and ICRF Waves in 3D Applications of Fusion Plasma Devices*. PhD thesis, École Polytechnique Fédérale de Lausanne, 2017.

[23] John Wesson and DJ Campbell. *Tokamaks*, volume 149. Oxford University Press, 2011.

[24] R. Koch. *Fus. Sci. Tech.*, 49:167–176, 2006.

[25] D. Cohen-Or and A. Kaufman. *Graphical Models and Image Processing*, 57(6):453–461, 1995.

[26] O. Asunta et al. *Comp. Phys. Comm.*, 188, 2015.

[27] A. Pankin et al. *Comp. Phys. Comms.*, 159(3):157 – 184, 2004.

[28] M. McMillan and S. A. Lazerson. *Plas. Phys. Cont. Fus.*, 2014.

[29] P. Helander. *Rep. Prog. Phys.*, 77(087001), 2014.

[30] H. E. Mynick. *Phys. Plas.*, 13, 2006.

[31] J. Ongena et al. *Phys. Plas.*, 21(6):061514, 2014.

[32] D. Pfefferlé, J.P. Graves, W.A. Cooper, C. Misev, I.T. Chapman, M. Turnyanskiy, and S. Sangaroon. Nbi fast ion confinement in the helical core of mast hybrid-like plasmas. *Nuclear Fusion*, 54(6):064020, 2014.

[33] J. Ongena et al. *EPJ Web. Conf.*, 157:02006, 2017.